Chinese Chemical Letters 34 (2023) 107683

Contents lists available at ScienceDirect

Chinese Chemical Letters

journal homepage: www.elsevier.com/locate/cclet

Cascaded electron transition proved by femto-second transient absorption spectroscopy for enhanced photocatalysis hydrogen generation

Xin Wang[a], Huiqian Jiang[a], Mingshan Zhu[b,*], Xiaowei Shi[a,*]

[a] Department of Applied Chemistry, Zhejiang University of Technology, Hangzhou 310031, China
[b] School of Environment, Jinan University, Guangzhou 511443, China

ARTICLE INFO

Article history:
Received 29 March 2022
Revised 2 July 2022
Accepted 14 July 2022
Available online 16 July 2022

Keywords:
Photocatalysis
Hydrogen generation
g-C_3N_4
Ternary heterostructure
Charge transfer

ABSTRACT

Regulating flow direction of photo-excited electrons from interior to active sites in surface is critical to enhance the photocatalytic performance. Herein, photoinduced chemical reduction process was utilized to pinpoint deposit CdS and NiS nanodots sequentially onto g-C_3N_4 nanosheets. The resulted hybrid composite NiS/CdS/g-C_3N_4 was much more active under visible light, and eventually boosted the hydrogen evolution rate of 3015 μmol g^{-1} h^{-1}, to be 2.4 folds better than that of g-C_3N_4. Because of the relative low content of CdS (around 3.0 wt%), the enhanced activity is due to the favoring band overlapping and promoting charge separation rather than increasing light absorption. Femto-second time-resolved transient absorption spectroscopy (fs-TAS) clearly reveals that the photo-excited electrons are from g-C_3N_4, and then migrate unidirectionally to CdS and finally to NiS, which is caused by the precisely regulate the position of CdS and NiS on g-C_3N_4 surface. This study elucidates the electron transfer kinetics and processes in multi-component system and affords a new avenue to construct stable photocatalysts with high activity.

Owing to the environmentally friendly and high specific energy of combustion (142 MJ/kg), hydrogen (H_2) is recognized as a promising candidate to manage the global carbon balance and remit the energy issues [1,2]. Developing low cost and efficient strategies to generate H_2 is thus highly desirable, in which solar light induced hydrogen evolution reaction (HER) has emerged for applications in this domain [3,4]. Generally, HER could only take place at sites on the surface of catalysts, and regulating charge transfer to inhibit their recombination is crucial for photocatalysis reaction [5–8]. Incorporating another semiconductor to form heterostructure is a widely accepted method due to the inducing of a build-in interfacial electric field through the energy band offset, which enables the reverse migration of photogenerated electrons and holes [9–12]. Accordingly, a variety of approaches, such as hydrothermal, mechanical mixing, and cation exchange, have been proposed and employed for synthesizing heterostructures [13,14]. While the obtained guest semiconductors are usually randomly dispersed on the host ones using these routes, and it is still difficult to control the electron transfer direction through precisely adjusting the positions of the second semiconductor.

Photochemical, a facile and rapid process for depositing noble metal nanoparticles on light-response substances, is commonly harnessed to fabricate catalysts in photocatalysis [15–17]. It has been proved that the photo-excited electrons (holes) generated in semiconductors could migrate to certain places to reduce some metal precursors, leading to the selectivity attachment of metal particles on substrate surface [18]. The resulted composite exhibits advantages in charge separation due to the regulation of excited electron flow direction compared with that prepared by traditional methods [19]. Inspired by this, photochemical process has also been extended from metals to semiconductors, and a series of CdS-based photocatalysts have been developed [20–22]. Among them, CdS/g-C_3N_4 catalyst is widely synthesized by many researchers [19,23]. While the fundamental photophysical processes have been poorly understood between the host and guest semiconductors, leading to the insufficient evidences to prove the type of CdS/g-C_3N_4 heterostructure (Z-Scheme or type II) [19,24]. More importantly, previous photoinduction obtained CdS-based catalysts usually contain high weight percent of CdS, and it is well known that CdS is an effective photocatalyst for HER [19,25]. Therefore, whether the enhanced catalytic activity of heterostructures comes

* Corresponding authors.
E-mail addresses: zhumingshan@jnu.edu.cn (M. Zhu), sxw20081990@zjut.edu.cn (X. Shi).

https://doi.org/10.1016/j.cclet.2022.07.026
1001-8417/

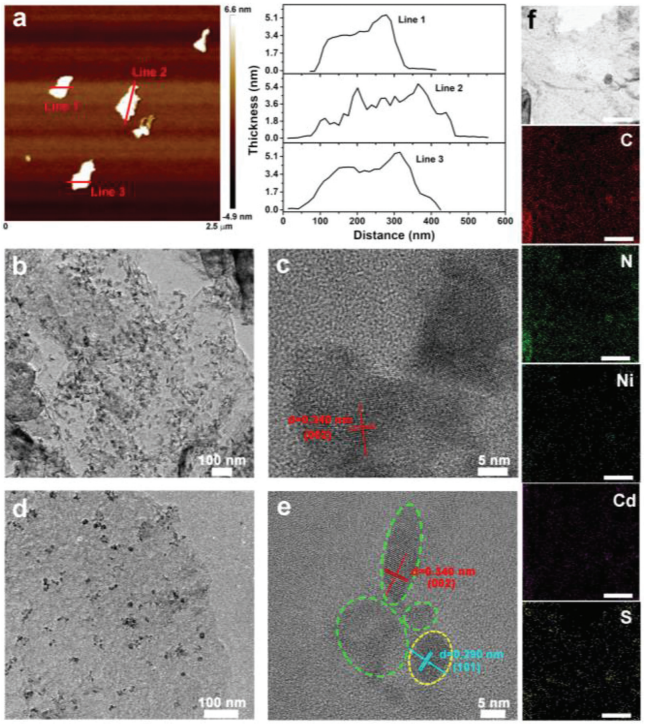

Fig. 1. (a) AFM image of g-C3N4 and their corresponding height. TEM (b) and HRTEM (c) images of CC-120. TEM (d) and HRTEM (e) images of CCN-25, the green circles refer to CdS and the yellow circle refers to NiS. (f) STEM-EDX images of CCN-25.

from the incorporated CdS or the facilitated charge separation also requires a deep discussion.

Even through the recombination of electron-hole pairs in heterostructure photocatalysts would be retarded, insufficient of active centers still hinders their performance [26,27]. Recently, typical transition metal sulfides, such as NiS, have been extensively regarded as promising candidates for electrocatalysis HER, and thus employed as cocatalysts in photocatalysis HER to replace precious noble metals (Pt, Pd, and Au) [28,29]. Herein, the ultrathin g-C_3N_4 nanosheets were used as substrate to build a ternary photocatalyst for HER by orderly photodepositing CdS and NiS. Due to the low content of CdS (around 3.0 wt%), most of the photo-excited electrons in CdS/g-C_3N_4 derive from g-C_3N_4. Moreover, the closely contact of NiS nanoparticles with CdS obviously demonstrated efficient electron transmission from g-C_3N_4 to CdS, where the sulfur precursors of NiS were reduced. The examined charge transfer dynamics and processes revealed a newly formed electron pathway in g-C_3N_4 after pinpoint anchoring CdS and NiS sequentially. The results showed that the photocatalytic activity of NiS/CdS/g-C_3N_4 was significantly superior to that of g-C_3N_4 and NiS/g-C_3N_4. This basic study of photophysical property provides guidance for the designing and synthesizing photocatalysts.

The surface morphology and structure of different photocatalysts were first characterized by TEM, and a general appearance of g-C_3N_4 was shown in Fig. S1 (Supporting information). It can be noticed that g-C_3N_4 displays a large-scale flexible two-dimensional (2D) structure. Due to the long-time thermally annealing under air atmosphere, the surface of g-C_3N_4 becomes rough and appears as nanosticks cross-linked with each other. According to AFM results, the thickness of g-C_3N_4 is measured to be less than 6 nm, suggesting an ultrathin layer structure (Fig. 1a). Then a photoinduction strategy was utilized to synthesize CdS/g-C_3N_4 heterostructures. Through altering the irradiation time, photocatalysts with different amount of CdS were achieved and named as CC-*X* (see Supporting information for details). Compared with pristine g-C_3N_4, CdS fine particles are separately and uniformly scattered on the surface of g-C_3N_4, and the particle size gradually increases from ~20 nm to ~80 nm with the prolonging of irradiation time (Fig. S2 in Supporting information). TEM and HRTEM images indicate that CdS nanoparticles are selectively attached onto g-C_3N_4 nanosheets without any aggregation, where the lattice fringe of 0.340 nm corresponds to the (002) facet of CdS (Figs. 1b and c) [30]. The close contact between g-C_3N_4 and CdS is beneficial to charge separation. After further depositing NiS, g-C_3N_4 still keeps a 2D layer structure without any morphology change (labeled as CCN-Y), as shown in Fig. 1d. It is found that two linked nanoparticles with lattice fringe spacing of 0.340 and 0.290 nm appear in HRTEM image, which are assigned to the (002) and (101) facet of CdS and NiS, respectively (circles in Fig. 1e) [31]. Additionally, no NiS nanoparticles individually grow on the surface of g-C_3N_4 (Fig. 1e and Fig. S3 in Supporting information). This result implies that the photoexcited electrons in g-C_3N_4 would effectively inject into CdS and then accumulate around CdS. The energy-dispersive spectroscopy (EDS) mappings in Fig. 1f confirm that CdS and NiS nanoparticles are uniformly distributed on the surface of g-C_3N_4 (Fig. 1f). These observations indicate that the photocatalyst prepared by photoinduction method possesses a heterostructure with designated electron transfer route and is not a simple physical mixture of separate phases.

The photocatalysts were then examined by XRD and FT-IR to determine their texture properties. The peak at 27.4° matches well with the (002) stacking layered structure of g-C_3N_4, and the 12.9° peak corresponds to (110) in-plane repeated unites (Fig. S4a in Supporting information) [32,33]. After photodeposition of CdS and NiS, the characteristic peaks of g-C_3N_4 are well preserved without any shift. While due to the low content and crystallinity, no diffraction peaks of CdS and NiS could be observed in XRD patterns. For the FT-IR spectra, all the peaks belonging to g-C_3N_4 are preserved without any change, demonstrating that g-C_3N_4 nanosheets could basically keep their crystal structure in heterostructures after photodeposition process (Fig. S4b in Supporting information).

The chemical composition and charge distribution of g-C_3N_4, CC-120, and CCN-25 were characterized by XPS. Fig. 2a illustrates the wide-scan XPS spectra of each photocatalyst, in which C 1s, N 1s, and small Cd 3d peaks could be identified. In the high resolution XPS spectrum, the peak of C 1s in g-C_3N_4 at 288.5 eV represents the sp^2-nonded carbon (N-C=N), while the peak at 285.4 eV refers to the graphitic carbon (C-C) groups in g-C_3N_4 (Fig. 2b). For the N 1s spectra, the deconvoluted peaks at 400.5, 399.5, and 398.9 eV are attributed to amino groups (C-N-H), N atoms in 3 heptazine units (N-$(C)_3$), and heptazine ring center (C=N-C), respectively (Fig. 2c) [34]. The peak at 405.5 eV assigning to a more oxidized nitrogen state is as well detected in previous work [35]. After the CdS/g-C_3N_4 heterostructure is formed, the characteristic peak positions of both C 1s and N 1s move toward higher binding energy, indicating that there is a strong interaction between g-C_3N_4 and CdS. Typically, the XPS peak position shifting to higher binding energy demonstrates the depletion of electrons around the atom, and the excited electrons in g-C_3N_4 are chiefly localized in C atoms since the C atoms mainly contribute to the bottom of conduction band [36,37]. Thus, the variations of C 1s in CC-120 and CCN-25 prove that the electrons could inject from g-C_3N_4 into CdS. The XPS peaks of Cd 3d at 412.7 and 405.8 eV are assigned to Cd $3d_{3/2}$ and $3d_{5/2}$ in CC-120, respectively (Fig. 2d). Interestingly, their positions also move to higher binding energy after forming CCN-25, proving the electron injection from CdS to NiS. The peaks at 163.9 and 162.2 eV are due to S^{2-} in CdS and NiS (Fig. 2e) [38]. The binding energy of two main peaks at 862.7 and 856.3 eV are in accordance with the Ni species in NiS (Fig. 2f). According to above analysis, CdS and NiS are confirmed to photochemically deposit

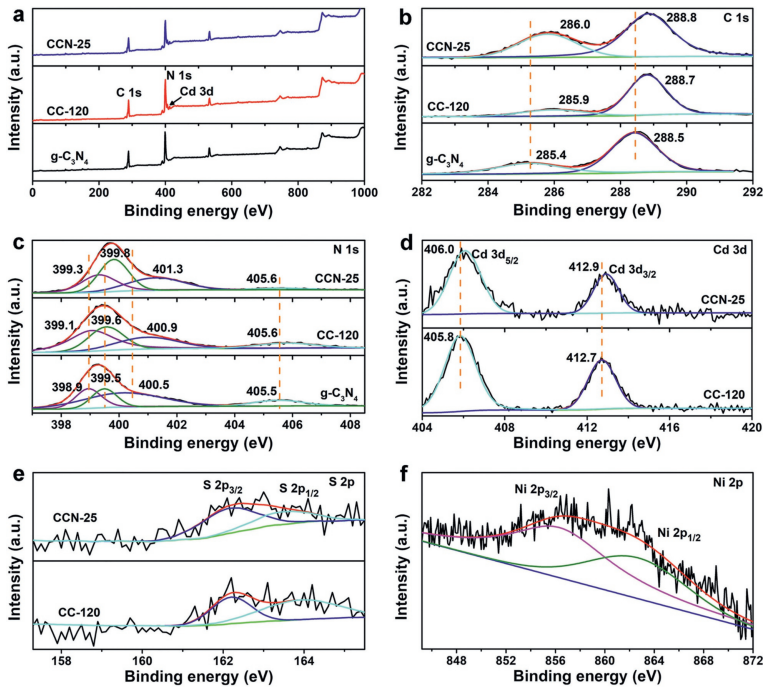

Fig. 2. XPS spectra of wide-scan (a), C 1s (b), N 1s (c) for g-C_3N_4, CC-120, and CCN-25. XPS spectra of Cd 3d (d) and S 2p (e) for CC-120 and CCN-25. XPS spectra of Ni 2p (f) for CCN-25.

onto g-C_3N_4 and an efficient charge migration could be observed [39–41]. In addition, the weight percent of NiS, CdS, and g-C_3N_4 in CCN-25 were also calculated, in which the amount of CdS was relatively low (around 3.0 wt%, Table S1 in Supporting information).

Fig. 3a shows the optical properties of individual photocatalysts, and the absorption edge of pristine g-C_3N_4 is approximately 440 nm, resulting in a bandgap (E_g) of 2.85 eV. Even though CdS shows a strong light absorption in the visible extent (450–550 nm, assigning to the bandgap of 2.23 eV, Fig. 3b), only a slightly red shift could be observed in CdS/g-C_3N_4. This phenomenon is quite different from previous work that the absorption behavior of heterostructure is significantly affected by the deposited CdS due to its large loading content [24]. After loading NiS nanoparticles, light absorption is gradually strengthened with the increasing amount of NiS precursors in the range of 500–800 nm, while the absorption edge of CCN-*Y* exhibits no change compared with that of CC-120. The corresponding digital images of different photocatalysts shown in Fig. S5 (Supporting information) obviously demonstrate the color change from pale white for g-C_3N_4 to grey for CCN-100. To explore the band structure, Mott-Schottky (M-S) plots were conducted, and the flat band potential values (E_{fb}) of CdS and g-C_3N_4 are −0.98 and −1.75 eV versus those of Ag/AgCl, respectively (Fig. S6 in Supporting information). The positive slopes of Mott-Schottky curves indicate that CdS and g-C_3N_4 are n-type semiconductors. In general, it is considered that the conduction band (E_{CB}) of n-type semiconductors is minus 0.1 eV compared with their E_{fb}. Therefore, the E_{CB} for CdS and g-C_3N_4 could be estimated as −0.48 and −1.25 eV *versus* reversible hydrogen electrode (*vs.* RHE), and their valence band potential (E_{VB}) are measured to be 1.75 and 1.60 eV corresponding to the equation: $E_{VB} = E_g + E_{CB}$, respectively (Fig. S7 in Supporting information).

Photocatalytic H_2 evolution reaction was put into effect at room temperature with TEOA (20 vol%) as a hole scavenger under the visible light irradiation ($\lambda > 400$ nm). Fig. 3c exhibits the results of H_2 production rate over g-C_3N_4 and different CC-*X* photocatalysts in aqueous suspensions with a certain amount of NiS as co-catalyst. Although NiS is introduced, pristine g-C_3N_4 still illustrates poor activity (1281 μmol g^{-1} h^{-1}), probably because of the rapid recombination of electron-hole pairs. While the photocatalytic activity is increased after combining CdS, and the amount of H_2 initially enhances and then gradually decreases with the prolonging irradiation time. Among them, CC-120 shows the highest photocatalytic performance. We suppose that the reduction of H_2 evolution for CC-180 and CC-240 would be the increased particle size of CdS, leading to the prohibition of charge transfer from the interior of CdS to surface and finally to NiS. Then, CC-120 photocatalyst was employed as substrate to detect the influences of photodeposited NiS on photocatalytic performance (Fig. 3c). The H_2 evolution rate is boosted with the increasing of NiS, and CCN-25 displays the highest activity with the value of 3015 μmol g^{-1} h^{-1}, to be probably 2.4 folds better than that of g-C_3N_4 with similar amount of NiS (Fig. 3d). Wavelength dependence of the apparent quantum efficiency (AQE) was also calculated using various band-pass filter under the same reaction conditions (Fig. 3e). The trend of AQE follows well with that of absorbance, and it reaches up to 9.5% and 5.9% at 400 and 420 nm, respectively. The stability of CCN-25 was also tested, and CCN-25 maintained its activity for H_2 evolution after three cycles (Fig. 3f). XRD patterns indicate that CCN-25 remains unchanged in the crystal structure (Fig. S8 in Supporting information). CdS and NiS nanoparticles could still be observed in HRTEM image and the elemental mappings of CCN-25 after the durability test also demonstrate that CdS and NiS nanoparticles are evenly dispersed on the surface of g-C_3N_4 without any aggregation (Figs. S9 and S10 in Supporting information).

Due to the low content of CdS in heterostructure based on above analysis and the well-kept appearance and layer-structure of g-C_3N_4 after photochemical reaction, the introduced CdS and surface area of CCN-Y would not cause the increment for H_2 evolution rate. We hypothesize that the efficient electron flow from g-C_3N_4 to CdS and ultimately to NiS is account for the enhanced activity. A series of photoelectrochemical measurements were performed to support the effect of such charge separation properties in heterostructures. The transient photocurrent (*I-t*) curves of several on-off cycles under intermittent visible-light irradiation in-

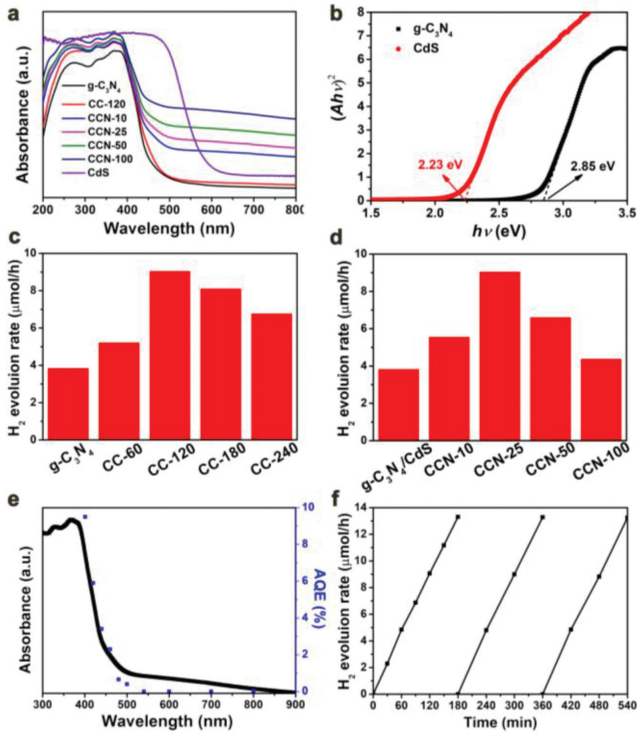

Fig. 3. (a) UV-vis absorption spectra of g-C_3N_4, CdS, CC-120, and CCN-Y. (b) Tauc's plots of CdS and g-C_3N_4. (c) Comparison of photocatalytic H_2 evolution activities of g-C_3N_4 and CC-X under visible light irradiation with a certain amount of NiS as co-catalyst. (d) Comparison of photocatalytic H_2 evolution activities of CdS/g-C_3N_4 and CCN-Y under visible light irradiation. (e) Wavelength dependence of the apparent quantum efficiency for CCN-25. (f) Cycling test of photocatalytic H2 evolution for CCN-25.

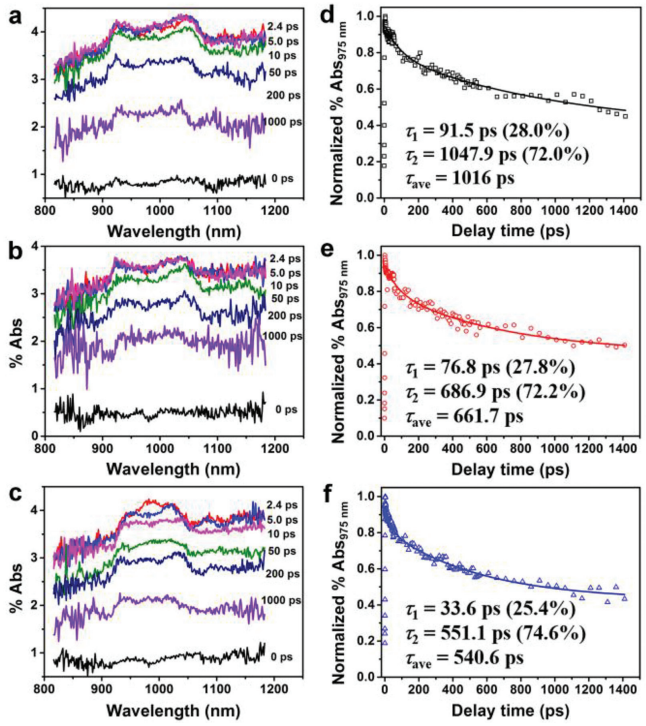

Fig. 4. Transient absorption spectra of pristine g-C_3N_4 (a), CC-120 (b), and CCN-25 (c) at different time delays following the excitation at 400 nm. The normalized time profiles of transient absorption at 975 nm for g-C_3N_4 (d), CC-120 (e), and CCN-25 (f). The time profiles were fitted according to the equation: $\Delta A = \Delta A_0 + \sum_i A_i e^{\left(-\frac{t}{\tau_i}\right)}$, where τ and A represent the lifetimes and amplitudes, respectively. The average lifetime (τ_{ave}) was acquired by calculation according to the equation: $\tau_{ave} = \sum_{i=1}^{i=n} A_i\tau_i^2 / \sum_{i=1}^{i=n} A_i\tau_i$.

dicate that g-C_3N_4 performs the highest photocurrent density of 1.76 μA/cm^2 after orderly photodepositing CdS and NiS, which is much higher than that of pristine g-C_3N_4 (0.25 μA/cm^2) and CC-120 (0.57 μA/cm^2) (Fig. S11a in Supporting information). The EIS Nyquist plots of g-C_3N_4, CC-120, and CCN-25 together with simulated equivalent electrical circuits were also provided in Figs. S11b and c (Supporting information), in which R_s and R_{ct} are electrolyte solution resistance and the interfacial charge-transfer resistance, respectively [42]. Based on the model, CCN-25 showed the smallest semicircle diameter and R_{ct} value (Table S2 in Supporting information), proving the lowest resistance of interfacial charge-transfer in CCN-25 [43,44]. Moreover, the efficient charge transfer in CCN-25 was also identified by photoluminescence (PL) spectroscopy (Fig. S12 in Supporting information). Contrary to previous works that the PL spectra of CdS/g-C_3N_4 could exhibit both emission peaks of g-C_3N_4 and CdS, the composites here only show PL emission peak of g-C_3N_4, also making clear that the photogenerated electrons in the heterostructures mainly derive from g-C_3N_4 [24]. Interestingly, the PL intensity greatly decreases after depositing CdS, and CCN-25 reveals the weakest intensity with a quenching intensity of about 70% compared to the undecorated g-C_3N_4.

According to above analyses, the retarded charge recombination in NiS/CdS/g-C_3N_4 has been proved. While the detailed electron transfer kinetics are still not obvious, which would provide direct evidence to determine the type of heterostructure and simultaneously explain the enhancement of photocatalytic activity. Therefore, femto-second transient diffuse reflectance (TDR), a robust tool for tracking the dynamics of charge carriers involved in nanostructured systems in real time, was measured to probe the average charge lifetimes and charge transfer processes. A pump pulse with a central wavelength of 400 nm was used to record the TDR spectra at different time delays, which is effective for exciting electrons from the valence band of g-C_3N_4 to the conduction band. An absorption signal, ranging from 900–1100 nm, is observed in g-C_3N_4, assigning to the trapped or free electrons in semiconductors (Fig. 4a) [45]. And it turns out that very similar TA spectra are yielded for CC-120 and CCN-25 (Figs. 4b and c). This result also proves that most of the photo-excited electrons are from g-C_3N_4. In addition, the transient absorption immediately reaches highest upon the excitation, and then gradually decays. Comparing to the pristine g-C_3N_4, the absorption of CC-120 within delay time of 2.4–200 ps decays more rapidly, while the CCN-25 discloses the fastest decay. The absorption-time profiles recorded at 975 nm for different photocatalysts are illustrated in Figs. 4d–f, which are fitted by a multi-exponential function. The pristine g-C_3N_4 exhibits a signal that can be characterized by two-time constants: $\tau_1 = 91.5$ ps (28.0%) and $\tau_2 = 1047.9$ ps (72.0%). The shorter lifetime caused by electrons trapped in the sub-state is attributed to the nonradiative recombination process, while the longer lifetime component is assigned to the recombination of excitons in semiconductors. The weighted average lifetime (τ_{ave}) of electron-hole pairs is 1016 ps. Notably, the fitting curve is converged to a long-lived plateau with a certain amplitude, reflecting that the charge recombination possesses a relative long lifetime up to nano- or microsecond. After decorating CdS, the composite also displays photoinduced absorption signals that can be characterized by two-time constants: $\tau_1 = 76.8$ ps (27.8%) and $\tau_2 = 686.9$ ps (72.2%), and the average lifetime is calculated to be 661.7 ps. The further shortened average recovery lifetime in CCN-25 (540.6 ps) is caused by the decreasing of τ_1 (33.6 ps, 25.4%) and τ_2 (551.1 ps, 74.6%). Commonly, the average lifetime is regarded as an important parameter to estimate the separation

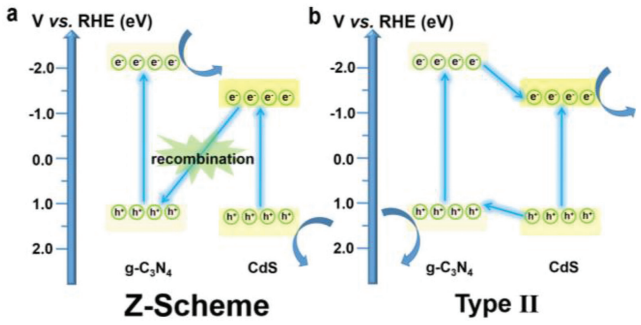

Fig. 5. Energy level diagrams and charge transfer channels of Z-Scheme (a) and type II heterostructure (b).

and transfer efficiency of photogenerated charge carriers in photocatalysts [31]. Such difference can be ascribed to the opening of an additional charge transfer channel in heterostructure. Therefore, the TDR results prove that a typical type II rather than a Z-Scheme heterostructure is formed here for the CdS/g-C_3N_4 composite.

In addition to fitting parameters of TDR spectra, the long stability of CCN-25 also excludes the Z-Scheme heterostructure between g-C_3N_4 and CdS. According to the band level calculations, the conduction band of CdS is lower than that of g-C_3N_4. If the Z-Scheme system was formed, electrons probably transfer from CdS to g-C_3N_4, leading to the recombination without any redox reactions (Fig. 5a). While the holes left on CdS would increase the light corrosion of CdS, which is contradict with the stability test. As a result, the proper mechanism of the reinforced photocatalytic HER performance for NiS/CdS/g-C_3N_4 heterostructure is put forward. Upon light irradiation, g-C_3N_4 is excited together with CdS. While due to the low amount of CdS, most of the photogenerated electrons come from g-C_3N_4. Then, the electrons in the interface states of g-C_3N_4 are injected into CdS and finally to NiS in an efficient manner, whereas the valence holes of CdS are transferred to the valence band of g-C_3N_4 (Fig. 5b). In consequence, the electrons possess more opportunities to participate in the proton reduction. Meanwhile, the photo-corrosion of CdS is also inhibited, resulting in the increase of stability and activity for H_2 evolution.

A precisely controlled electron flow direction is achieved through pinpoint depositing CdS and NiS subsequently on g-C_3N_4 thin layers *via* photochemical strategy. From tracking of the charge migration based on TDR and PL spectroscopy, the electrons prefer transferring from g-C_3N_4 to CdS and ultimately NiS stepwise, and a typical type II heterostructure is constructed in CdS/g-C_3N_4. Because of the efficient charge separation, the photocatalyst exhibits an obvious enhanced catalytic activity for H_2 evolution under visible light irradiation (3015 μmol g^{-1} h^{-1}) with introducing a low content of CdS (~3.0 wt%), to be approximately 2.4-fold comparing to the pristine g-C_3N_4. Additionally, the composite also possesses superior resistance for the photocorrosion of CdS. The work here systematically studies the connection between g-C_3N_4 and CdS, which may provide a choice to design and fabricate ideal heterojunction with regulated charge migration positions.

Declaration of competing interest

The authors declare that they have no known competing financial interests or personal relationships that could have appeared to influence the work reported in this paper.

Acknowledgment

This work is supported by the National Natural Science Foundation of China (No. 21902143).

Supplementary materials

Supplementary material associated with this article can be found, in the online version, at doi:10.1016/j.cclet.2022.07.026.

References

[1] T. Sun, S. Mitchell, J. Li, et al., Adv. Mater. 33 (2021) 2003075.
[2] H. Luo, J. Barrio, N. Sunny, et al., Adv. Energy Mater. 11 (2021) 2101180.
[3] Y. Wang, J. Mao, X. Meng, et al., Chem. Rev. 119 (2019) 1806–1854.
[4] L. Pan, S. Sun, Y. Chen, et al., Adv. Energy Mater. 10 (2020) 2000214.
[5] X.H. Jiang, L.S. Zhang, H.Y. Liu, et al., Angew. Chem. Int. Ed. 59 (2020) 23112–23116.
[6] W. Jiang, Y. Zhao, X. Zong, et al., Angew. Chem. Int. Ed. 60 (2021) 6124–6129.
[7] X. Shi, L. Mao, C. Dai, et al., J. Mater. Chem. A 8 (2020) 13376–13384.
[8] Z. Wang, Y. Luo, T. Hisatomi, et al., Nat. Commun. 12 (2021) 1005.
[9] X. Shi, M. Fujitsuka, Z. Lou, et al., J. Mater. Chem. A 5 (2017) 9671–9681.
[10] B. Lin, H. Li, H. An, et al., Appl. Catal. B: Environ. 220 (2018) 542–552.
[11] Y. Chao, P. Zhou, N. Li, et al., Adv. Mater. 31 (2019) 1807226.
[12] S. Huang, T. Ouyang, B. Zheng, et al., Angew. Chem. Int. Ed. 60 (2021) 9546–9552.
[13] J. Ran, W. Guo, H. Wang, et al., Adv. Mater. 30 (2018) 1800128.
[14] S. Huang, B. Zheng, Z. Tang, et al., Chem. Eng. J. 422 (2021) 130086.
[15] X. Pan, X. Chen, Z. Yi, ACS Appl. Mater. Interfaces 8 (2016) 10104–10108.
[16] V.C. Nguyen, D.B. Nimbalkar, L.D. Nam, et al., ACS Catal. 11 (2021) 4955–4967.
[17] J. Wei, M. Cao, K. Xiao, et al., Small Struct. 2 (2021) 2100047.
[18] K. Wenderich, G. Mul, Chem. Rev. 116 (2016) 14587–14619.
[19] W. Jiang, X. Zong, L. An, et al., ACS Catal. 8 (2018) 2209–2217.
[20] H. Tada, M. Fujishima, H. Kobayashi, Chem. Soc. Rev. 40 (2011) 4232–4243.
[21] H. Fujiwara, H. Hosokawa, K. Murakoshi, et al., J. Phys. Chem. B 101 (1997) 8270–8278.
[22] Q. Liu, X. He, J. Tao, et al., ChemNanoMat 7 (2021) 44–49.
[23] W. Li, C. Feng, S. Dai, et al., Appl. Catal. B: Environ. 168-169 (2015) 465–471.
[24] L. Chen, Y. Xu, B. Chen, Appl. Catal. B: Environ. 256 (2019) 117848.
[25] L. Cheng, Q. Xiang, Y. Liao, et al., Energy Environ. Sci. 11 (2018) 1362–1391.
[26] D. Chen, Z. Liu, Z. Guo, et al., ChemSusChem 12 (2019) 3286–3295.
[27] X. Shi, F. Dong, C. Dai, et al., Electrochim. Acta 361 (2020) 137017.
[28] H. Zhao, H. Zhang, G. Cui, et al., Appl. Catal. B: Environ. 225 (2018) 284–290.
[29] Y. Guan, Y. Feng, J. Wan, et al., Small 14 (2018) 1800697.
[30] R. Shi, H.F. Ye, F. Liang, et al., Adv. Mater. 30 (2018) 1705941.
[31] A. Yan, X. Shi, F. Huang, et al., Appl. Catal. B: Environ. 250 (2019) 163–170.
[32] Q. Han, B. Wang, Y. Zhao, et al., Angew. Chem. Int. Ed. 54 (2015) 11433–11437.
[33] X. Xiao, Y. Gao, L. Zhang, et al., Adv. Mater. 32 (2020) 2003082.
[34] C. Li, Y. Du, D. Wang, et al., Adv. Funct. Mater. 27 (2017) 1604328.
[35] L. Kong, Y. Ji, Z. Dang, et al., Adv. Funct. Mater. 28 (2018) 1800668.
[36] Y. Ma, M. Chen, H. Geng, et al., Adv. Funct. Mater. 30 (2020) 2000561.
[37] X. Jiang, L. Zhang, H. Liu, et al., Angew. Chem. Int. Ed. 59 (2020) 23112–23116.
[38] X. Shi, S. Kim, M. Fujitsuka, et al., Appl. Catal. B: Environ. 254 (2019) 594–600.
[39] B. Xu, S. Qi, F. Li, et al., Chin. Chem. Lett. 31 (2020) 217–222.
[40] D. Yuan, M. Sun, S. Tang, et al., Chin. Chem. Lett. 31 (2020) 547–550.
[41] O. Ting, Y. Ye, C. Wu, et al., Angew. Chem. Int. Ed. 58 (2019) 4923–4928.
[42] W. Jiang, X Zong, L. An, et al., ACS Catal. 8 (2018) 2209–2217.
[43] Q. Zhao, J. Sun, S. Li, et al., ACS Catal. 8 (2018) 11863–11874.
[44] D. Li, H. Wang, H. Tang, et al., ACS Sustain. Chem. Eng. 7 (2019) 8466–8474.
[45] X. Shi, C. Dai, X. Wang, et al., Nat. Commun. 13 (2022) 1287.